Laplacian Pyramid Reconstruction and Refinement for Semantic Segmentation

Golnaz Ghiasi and Charless C. Fowlkes
{gghiasi,fowlkes}@ics.uci.edu

Dept. of Computer Science,
University of California, Irvine

Abstract. CNN architectures have terrific recognition performance but rely on spatial pooling which makes it difficult to adapt them to tasks that require dense, pixel-accurate labeling. This paper makes two contributions: (1) We demonstrate that while the apparent spatial resolution of convolutional feature maps is low, the high-dimensional feature representation contains significant sub-pixel localization information. (2) We describe a multi-resolution reconstruction architecture based on a Laplacian pyramid that uses skip connections from higher resolution feature maps and multiplicative gating to successively refine segment boundaries reconstructed from lower-resolution maps. This approach yields state-of-the-art semantic segmentation results on the PASCAL VOC and Cityscapes segmentation benchmarks without resorting to more complex random-field inference or instance detection driven architectures.

Keywords: Semantic Segmentation, Convolutional Neural Networks

1 Introduction

Deep convolutional neural networks (CNNs) have proven highly effective at semantic segmentation due to the capacity of discriminatively pre-trained feature hierarchies to robustly represent and recognize objects and materials. As a result, CNNs have significantly outperformed previous approaches (e.g., [28,3,2]) that relied on hand-designed features and recognizers trained from scratch. A key difficulty in the adaption of CNN features to segmentation is that feature pooling layers, which introduce invariance to spatial deformations required for robust recognition, result in high-level representations with reduced spatial resolution. In this paper, we investigate this *spatial-semantic uncertainty principle* for CNN hierarchies (see Fig.1) and introduce two techniques that yield substantially improved segmentations.

First, we tackle the question of how much spatial information is represented at high levels of the feature hierarchy. A given spatial location in a convolutional feature map corresponds to a large block of input pixels (and an even larger "receptive field"). While max pooling in a single feature channel clearly destroys spatial information in that channel, spatial filtering prior to pooling introduces strong correlations across channels which could, in principle, encode
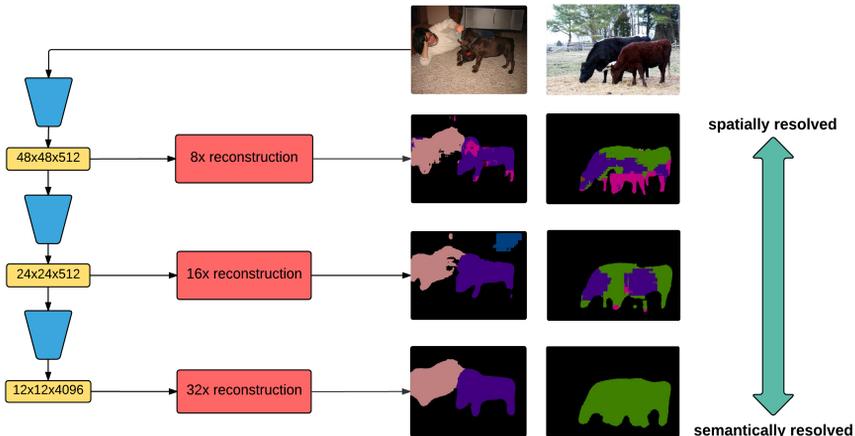
Fig. 1. In this paper, we explore the trade-off between spatial and semantic accuracy within CNN feature hierarchies. Such hierarchies generally follow a spatial-semantic uncertainty principle in which high levels of the hierarchy make accurate semantic predictions but are poorly localized in space while at low levels, boundaries are precise but labels are noisy. We develop reconstruction techniques for increasing spatial accuracy at a given level and refinement techniques for fusing multiple levels that limit these tradeoffs and produce improved semantic segmentations.

significant "sub-pixel" spatial information across the high-dimensional vector of sparse activations. We show that this is indeed the case and demonstrate a simple approach to spatial decoding using a small set of data-adapted basis functions that substantially improves over common upsampling schemes (see Fig. 2).

Second, having squeezed more spatial information from a given layer of the hierarchy, we turn to the question of fusing predictions across layers. A standard approach has been to either concatenate features (e.g., [15]) or linearly combine predictions (e.g., [24]). Concatenation is appealing but suffers from the high dimensionality of the resulting features. On the other hand, additive combinations of predictions from multiple layers does not make good use of the relative spatial-semantic content tradeoff. High-resolution layers are shallow with small receptive fields and hence yield inherently noisy predictions with high pixel-wise loss. As a result, we observe their contribution is significantly down-weighted relative to low-resolution layers during linear fusion and thus they have relatively little effect on final predictions.

Inspired in part by recent work on residual networks [16,17], we propose an architecture in which predictions derived from high-resolution layers are only required to correct residual errors in the low-resolution prediction. Importantly, we use multiplicative gating to avoid integrating (and hence penalizing) noisy high-resolution outputs in regions where the low-resolution predictions are confident about the semantic content. We call our method *Laplacian Pyramid Reconstruction and Refinement* (LRR) since the architecture uses a Laplacian reconstruc-
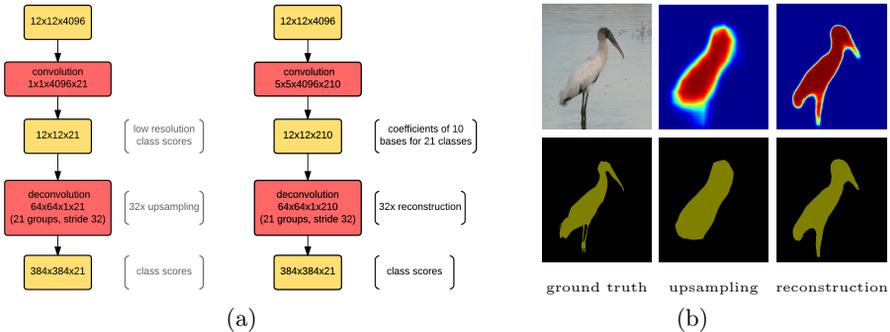
Fig. 2. (a) Upsampling architecture for FCN32s network (left) and our 32x reconstruction network (right). (b) Example of Class conditional probability maps and semantic segmentation predictions from FCN32s which performs upsampling (middle) and our 32x reconstruction network (right).

tion pyramid [1] to fuse predictions. Indeed, the class scores predicted at each level of our architecture typically look like bandpass decomposition of the full resolution segmentation mask (see Fig. 3).

2 Related Work

The inherent lack of spatial detail in CNN feature maps has been attacked using a variety of techniques. One insight is that spatial information lost during max-pooling can in part be recovered by unpooling and deconvolution [36] providing a useful way to visualize input dependency in feed-forward models [35]. This idea has been developed using learned deconvolution filters to perform semantic segmentation [26]. However, the deeply stacked deconvolutional output layers are difficult to train, requiring multi-stage training and more complicated object proposal aggregation.

A second key insight is that while activation maps at lower-levels of the CNN hierarchy lack object category specificity, they do contain higher spatial resolution information. Performing classification using a "jet" of feature map responses aggregated across multiple layers has been successfully leveraged for semantic segmentation [24], generic boundary detection [32], simultaneous detection and segmentation [15], and scene recognition [33]. Our architecture shares the basic skip connections of [24] but uses multiplicative, confidence-weighted gating when fusing predictions.

Our techniques are complementary to a range of other recent approaches that incorporate object proposals [10,26], attentional scale selection mechanisms [7], and conditional random fields (CRF) [5,21,23]. CRF-based methods integrate CNN score-maps with pairwise features derived from superpixels [9,25] or generic boundary detection [19,4] to more precisely localize segment boundaries. We demonstrate that our architecture works well as a drop in unary potential in fully connected CRFs [20] and would likely further benefit from end-to-end training [37].
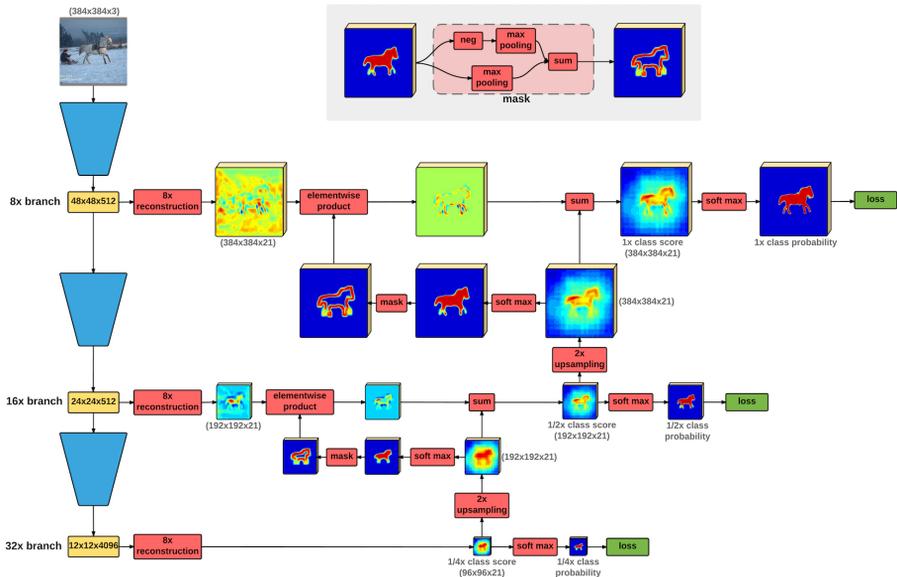
Fig. 3. Overview of our Laplacian pyramid reconstruction network architecture. We use low-resolution feature maps in the CNN hierarchy to reconstruct a coarse, low-frequency segmentation map and then refine this map by adding in higher frequency details derived from higher-resolution feature maps. Boundary masking (inset) suppresses the contribution of higher resolution layers in areas where the segmentation is confident, allowing the reconstruction to focus on predicting residual errors in uncertain areas (e.g., precisely localizing object boundaries). At each resolution layer, the reconstruction filters perform the same amount of upsampling which depends on the number of layers (e.g., our LRR-4x model utilizes 4x reconstruction on each of four branches). Standard 2x bilinear upsampling is applied to each class score map before combining it with higher resolution predictions.

3   Reconstruction with learned basis functions

A standard approach to predicting pixel class labels is to use a linear convolution to compute a low-resolution class score from the feature map and then upsample the score map to the original image resolution. A bilinear kernel is a suitable choice for this upsampling and has been used as a fixed filter or an initialization for the upsampling filter [15,24,5,37,7,10,13]. However, upsampling low-resolution class scores necessarily limits the amount of detail in the resulting segmentation (see Fig. 2 (a)) and discards any sub-pixel localization information that might be coded across the many channels of the low-resolution feature map. The simple fix of upsampling the feature map prior to classification poses computational difficulties due to the large number of feature channels (e.g. 4096). Furthermore, (bilinear) upsampling commutes with 1x1 convolutions used for class prediction so performing per-pixel linear classification on an up-

sampled feature map would yield equivalent results unless additional rounds of (non-linear) filtering were carried out on the high-resolution feature map.

To extract more detailed spatial information, we avoid immediately collapsing the high-dimensional feature map down to low-resolution class scores. Instead, we express the spatial pattern of high-resolution scores using a linear combination of high-resolution basis functions whose coefficients are predicted from the feature map (see Fig. 2 (a)). We term this approach "reconstruction" to distinguish it from the standard upsampling (although bilinear upsampling can clearly be seen as special case with a single basis function).

Reconstruction by deconvolution: In our implementation, we tile the high-resolution score map with overlapping basis functions (e.g., for 4x upsampled reconstruction we use basis functions with an 8x8 pixel support and a stride of 4). We use a convolutional layer to predict K basis coefficients for each of C classes from the high-dimensional, low-resolution feature map. The group of coefficients for each spatial location and class are then multiplied by the set of basis function for the class and summed using a standard deconvolution (convolution transpose) layer.

To write this explicitly, let s denote the stride, $q_s(i) = \lfloor \frac{i}{s} \rfloor$ denote the quotient, and $m_s(i) = i \bmod s$ the remainder of i by s. The reconstruction layer that maps basis coefficients $X \in \mathbb{R}^{H \times W \times K \times C}$ to class scores $Y \in \mathbb{R}^{sH \times sW \times C}$ using basis functions $B \in \mathbb{R}^{2s \times 2s \times K \times C}$ is given by:

$$Y_c[i,j] = \sum_{k=0}^{K-1} \sum_{(u,v) \in \{0,1\}^2} B_{k,c}\left[m_s(i) + s \cdot u, m_s(j) + s \cdot v\right] \cdot X_{k,c}\left[q_s(i) - u, q_s(j) - v\right]$$

where $B_{k,c}$ contains the k-th basis function for class c with corresponding spatial weights $X_{k,c}$. We assume $X_{k,c}$ is zero padded and Y_c is cropped appropriately.

Connection to spline interpolation: We note that a classic approach to improving on bilinear interpolation is to use a higher-order spline interpolant built from a standard set of non-overlapping polynomial basis functions where the weights are determined analytically to assure continuity between neighboring patches. Our approach using learned filters and basis functions makes minimal assumptions about mapping from high dimensional activations to the coefficients X but also offers no guarantees on the continuity of Y. We address this in part by using larger filter kernels (i.e., $5 \times 5 \times 4096$) for predicting the coefficients $X_{k,c}$ from the feature activations. This mimics the computation used in spline interpolation of introducing linear dependencies between neighboring basis weights and empirically improves continuity of the output predictions.

Learning basis functions: To leverage limited amounts of training data and speed up training, we initialize the deconvolution layers with a meaningful set of filters estimated by performing PCA on example segment patches. For this purpose, we extract 10000 patches for each class from training data where each patch is of size 32×32 and at least 2% of the patch pixels are members of
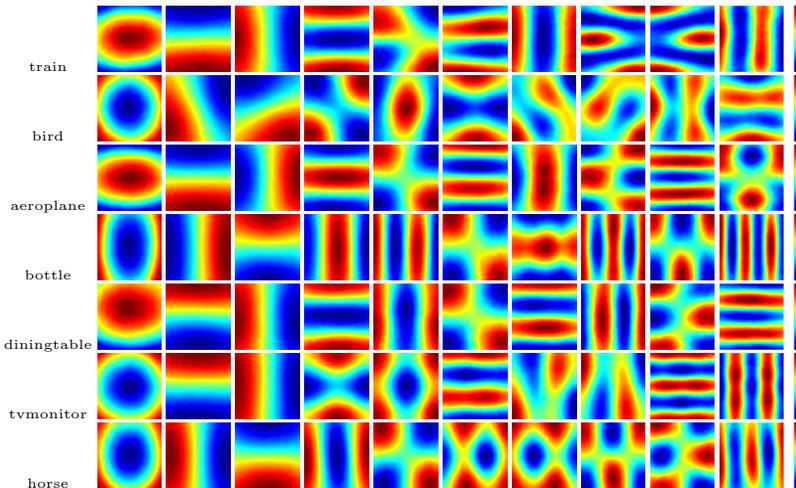
Fig. 4. Category-specific basis functions for reconstruction are adapted to modeling the shape of a given object class. For example, airplane segments tend to be elongated in the horizontal direction while bottles are elongated in the vertical direction.

the class. We apply PCA on the extracted patches to compute a class specific set of basis functions. Example bases for different categories of PASCAL VOC dataset are shown in Fig. 4. Interestingly, there is some significant variation among classes due to different segment shape statistics. We found it sufficient to initialize the reconstruction filters for different levels of the reconstruction pyramid with the same basis set (downsampled as needed). In both our model and the FCN bilinear upsampling model, we observed that end-to-end training resulted in insignificant ($< 10^{-7}$) changes to the basis functions.

We experimented with varying the resolution and number of basis functions of our reconstruction layer built on top of the ImageNet-pretrained VGG-16 network. We found that 10 functions sampled at a resolution of 8×8 were sufficient for accurate reconstruction of class score maps. Models trained with more than 10 basis functions commonly predicted zero weight coefficients for the higher-frequency basis functions. This suggests some limit to how much spatial information can be extracted from the low-res feature map (i.e., roughly 3x more than bilinear). However, this estimate is only a lower-bound since there are obvious limitations to how well we can fit the model. Other generative architectures (e.g., using larger sparse dictionaries) or additional information (e.g., max pooling "switches" in deconvolution [36]) may do even better.

4   Laplacian Pyramid Refinement

The basic intuition for our multi-resolution architecture comes from Burt and Adelson's classic Laplacian Pyramid [1], which decomposes an image into disjoint frequency bands using an elegant recursive computation (analysis) that produces
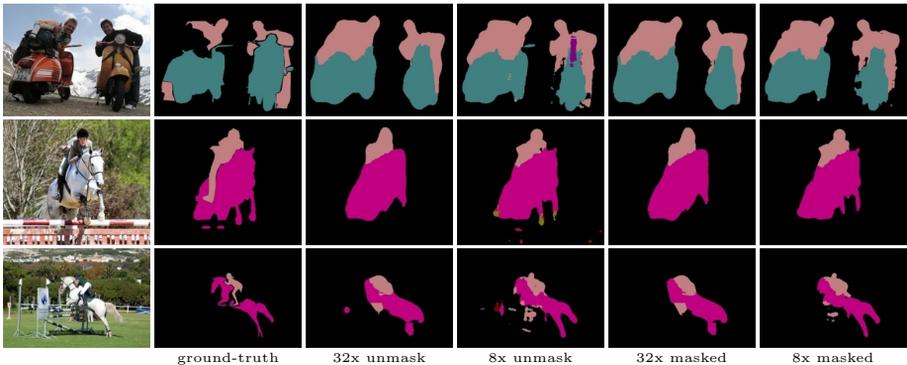
| | ground-truth | 32x unmask | 8x unmask | 32x masked | 8x masked |

Fig. 5. Visualization of segmentation results produced by our model with and without boundary masking. For each row, we show the input image, ground-truth and the segmentation results of 32x and 8x layers of our model without masking (middle) and with masking (right). The segmentation results for 8x layer of the model without masking has some noise not present in the 32x output. Masking allows such noise to be repressed in regions where the 32x outputs have high confidence.

appropriately down-sampled sub-bands such that the sum of the resulting sub-bands (synthesis) perfectly reproduces the original image. While the notion of frequency sub-bands is not appropriate for the non-linear filtering performed by standard CNNs, casual inspection of the response of individual activations to shifted input images reveals a power spectral density whose high-frequency components decay with depth leaving primarily low-frequency components (with a few high-frequency artifacts due to disjoint bins used in pooling). This suggests the possibility that the standard CNN architecture could be trained to serve the role of the analysis pyramid (predicting sub-band coefficients) which could then be assembled using a synthesis pyramid to estimate segmentations.

Figure 3 shows the overall architecture of our model. Starting from the coarse scale "low-frequency" segmentation estimate, we carry out a sequence of successive refinements, adding in information from "higher-frequency" sub-bands to improve the spatial fidelity of the resulting segmentation masks. For example, since the 32x layer already captures the coarse-scale support of the object, prediction from the 16x layer does not need to include this information and can instead focus on adding finer scale refinements of the segment boundary. [1]

Boundary masking: In practice, simply upsampling and summing the outputs of the analysis layers does not yield the desired effect. Unlike the Laplacian image analysis pyramid, the high resolution feature maps of the CNN do not have the "low-frequency" content subtracted out. As Fig.1 shows, high-resolution layers still happily make "low-frequency" predictions (e.g., in the middle of a large seg-

---

[1] Closely related architectures were used in [11] for generative image synthesis where the output of a lower-resolution model was used as input for a CNN which predicted an additive refinement, and in [27], where fusing and refinement across levels was carried out via concatenation followed by several convolution+ReLU layers.

VOC 2011-val	pixel acc.	mean acc.	mean IoU
FCN-32s	89.1%	73.3%	59.4%
FCN-16s	90.0%	75.7%	62.4%
FCN-8s	90.3%	75.9%	62.7%
LRR-32x (w/o aug)	90.7%	78.9%	64.1%
LRR-32x	91.5%	81.6%	66.8%
LRR-16x	91.8%	81.6%	67.8%
LRR-8x	92.4%	83.2%	69.5%
LRR-4x	92.2%	83.7%	69.0%
LRR-4x-ms	92.8%	84.6%	71.4%

Fig. 6. Comparison of our segment reconstruction model, LRR (without boundary masking) and the baseline FCN model[24] which uses upsampling. We find consistent benefits from using a higher-dimensional reconstruction basis rather than upsampling class prediction maps. We also see improved performance from using multi-scale training augmentation, fusing multiple feature maps, and running on multiple scales at test time. Note that the performance benefit of fusing multiple resolution feature maps diminishes with no gain or even decrease performance from adding in the 4x layer. Boundary masking (cf. Fig.7) allows for much better utilization of these fine scale features.

ment) even though they are often incorrect. As a result, in an architecture that simply sums together predictions across layers, we found the learned parameters tend to down-weight the contribution of high-resolution predictions to the sum in order to limit the potentially disastrous effect of these noisy predictions. However, this hampers the ability of the high-resolution predictions to significantly refine the segmentation in areas containing high-frequency content (i.e., segment boundaries).

To remedy this, we introduce a masking step that serves to explicitly subtract out the "low-frequency" content from the high-resolution signal. This takes the form of a multiplicative gating that prevents the high-resolution predictions from contributing to the final response in regions where lower-resolution predictions are confident. The inset in Fig.3 shows how this boundary mask is computed by using a max pooling operation to dilate the confident foreground and background predictions and taking their difference to isolate the boundary. The size of this dilation (pooling size) is tied to the amount of upsampling between successive layers of the pyramid, and hence fixed at 9 pixels in our implementation.

5   Experiments

We now describe a number of diagnostic experiments carried out using the PASCAL VOC [12] semantic segmentation dataset. In these experiments, models were trained on training/validation set split specified by [14] which includes 11287 training images and 736 held out validation images from the PASCAL 2011 val set. We focus primarily on the average Intersection-over-Union (IoU) metric which generally provides a more sensitive performance measure than per-pixel or per-class accuracy. We conduct diagnostic experiments on the model architecture using this validation data and test our final model via submission to the PASCAL VOC 2012 test data server, which benchmarks on an additional

VOC 2011-val	VOC			VOC+COCO			
	VGG-16			VGG-16			ResNet
	unmasked	masked	masked+DE	umasked	masked	masked+DE	masked+DE
LRR-4x(32x)	67.1%	67.0%	68.8%	71.3%	71.2%	72.9%	76.7%
LRR-4x(16x)	68.6%	69.2%	70.0%	72.1%	72.4%	73.9%	78.0%
LRR-4x(8x)	69.3%	70.3%	70.9%	72.9%	73.4%	74.9%	78.3%
LRR-4x	69.3%	70.5%	71.1%	72.9%	73.6%	75.1%	78.4%
LRR-4x-ms	71.9%	73.0%	73.6%	74.0%	75.0%	76.6%	79.2%
LRR-4x-ms-crf	73.2%	74.1%	74.6%	75.0%	76.1%	77.5%	79.9%

Fig. 7. Mean intersection-over-union (IoU) accuracy for intermediate outputs at different levels of our Laplacian reconstruction architecture trained with and without boundary masking (value in parentheses denotes an intermediate output of the full model). Masking allows us to squeeze additional gains out of high-resolution feature maps by focusing only on low-confidence areas near segment boundaries. Adding dilation and erosion losses (DE) to the 32x branch improves the accuracy of 32x predictions and as a result the overall performance. Running the model at multiple scales and performing post-processing using a CRF yielded further performance improvements.

set of 1456 images. We also report test benchmark performance on the recently released Cityscapes [8] dataset.

5.1 Parameter Optimization

We augment the layers of the ImageNet-pretrained VGG-16 network [29] or ResNet-101 [16] with our LRR architecture and fine-tune all layers via backpropagation. All models were trained and tested with Matconvnet [31] on a single NVIDIA GPU. We use standard stochastic gradient descent with batch size of 20, momentum of 0.9 and weight decay of 0.0005. The models and code are available at https://github.com/golnazghiasi/LRR.

Stage-wise training: Our 32x branch predicts a coarse semantic segmentation for the input image while the other branches add in details to the segmentation prediction. Thus 16x, 8x and 4x branches are dependent on 32x branch prediction and their task of adding details is meaningful only when 32x segmentation predictions are good. As a result we first optimize the model with only 32x loss and then add in connections to the other layers and continue to fine tune. At each layer we use a pixel-wise softmax log loss defined at a lower image resolution and use down-sampled ground-truth segmentations for training. For example, in LRR-4x the loss is defined at 1/8, 1/4, 1/2 and full image resolution for the 32x, 16x, 8x and 4x branches, respectively.

Dilation erosion objectives: We found that augmenting the model with branches to predict dilated and eroded class segments in addition of the original segments helps guide the model in predicting more accurate segmentation. For each training example and class, we compute a binary segmentation using the ground-truth and then compute its dilation and erosion using a disk with radius of 32 pixels. Since dilated segments of different classes are not mutually exclusive, a k-way soft-max is not appropriate so we use logistic loss instead. We
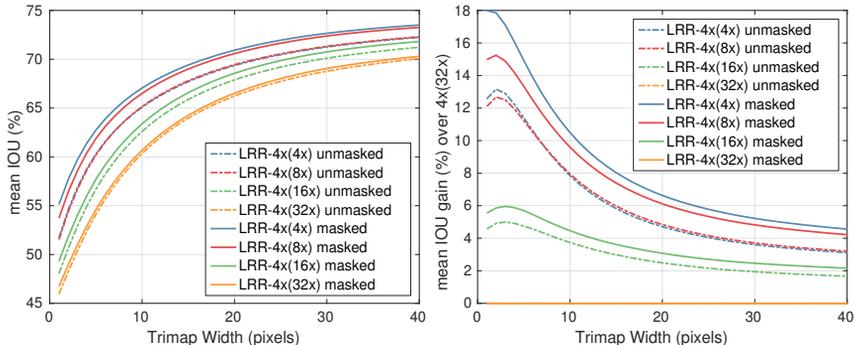
Fig. 8. The benefit of Laplacian pyramid boundary refinement becomes even more apparent when focusing on performance near object boundaries. Plots show segmentation performance within a thin band around the ground-truth object boundaries for intermediate predictions at different levels of our reconstruction pyramid. (right) Measuring accuracy or mean IoU relative to the baseline 32x output shows that the high-resolution feature maps are most valuable near object boundaries while masking improves performance both near and far from boundaries.

add these Dilation and Erosion (DE) losses to the 32x branch (at 1/8 resolution) when training LRR-4x. Adding these losses increased mean IoU of the 32x branch predictions from 71.2% to 72.9% and also the overall multi-scale accuracy from 75.0% to 76.6 (see Fig.7, built on VGG-16 and trained on VOC+COCO).

Multi-scale Data Augmentation: We augmented the training data with multiple scaled versions of each training examples. We randomly select an image size between 288 to 704 for each batch and then scale training examples of that batch to the selected size. When the selected size is larger than 384, we crop a window with size of 384×384 from the scaled image. This augmentation is helpful in improving the accuracy of the model and increased mean IoU of our 32x model from 64.07% to 66.81% on the validation data (see Fig.6).

5.2   Reconstruction vs Upsampling

To isolate the effectiveness of our proposed reconstruction method relative to simple upsampling, we compare the performance of our model without masking to the fully convolutional net (FCN) of [24]. For this experiment, we trained our model without scale augmentation using exactly same training data used for training the FCN models. We observed significant improvement over upsampling using reconstruction with 10 basis filters. Our 32x reconstruction model (w/o aug) achieved a mean IoU of 64.1% while FCN-32s and FCN-8s had a mean IoU of 59.4% and 62.7%, respectively (Fig. 6).

5.3 Multiplicative Masking and Boundary Refinement

We evaluated whether masking the contribution of high-resolution feature maps based on the confidence of the lower-resolution predictions resulted in better performance. We anticipated that this multiplicative masking would serve to remove noisy class predictions from high-resolution feature maps in high-confidence interior regions while allowing refinement of segment boundaries. Fig. 5 demonstrates the qualitative effect of boundary masking. While the prediction from the 32x branch is similar for both models (relatively noise free), masking improves the 8x prediction noticeably by removing small, incorrectly labeled segments while preserving boundary fidelity. We compute mean IoU benchmarks for different intermediate outputs of our LRR-4x model trained with and without masking (Table 7). Boundary masking yields about 1% overall improvement relative to the model without masking across all branches.

Evaluation near Object Boundaries: Our proposed model uses the higher resolution feature maps to refine the segmentation in the regions close to the boundaries, resulting in a more detailed segmentation (see Fig. 11). However, boundaries constitute a relatively small fraction of the total image pixels, limiting the impact of these improvements on the overall IoU performance benchmark (see, e.g. Fig. 7). To better characterize performance differences between models, we also computed mean IoU restricted to a narrow band of pixels around the ground-truth boundaries. This partitioning into figure/boundary/background is sometimes referred to as a tri-map in the matting literature and has been previously utilized in analyzing semantic segmentation performance [5,18].

Fig. 8 shows the mean IoU of our LRR-4x as a function of the width of the tri-map boundary zone. We plot both the absolute performance and performance relative to the low-resolution 32x output. As the curves confirm, adding in higher resolution feature maps results in the most performance gain near object boundaries. Masking improves performance both near and far from boundaries. Near boundaries masking allows for the higher-resolution layers to refine the boundary shape while far from boundaries the mask prevents those high-resolution layers from corrupting accurate low-resolution predictions.

5.4 CRF Post-processing

To show our architecture can easily be integrated with CRF-based models, we evaluated the use of our LRR model predictions as a unary potential in a fully-connected CRF [20,4]. We resize each input image to three different scales (1,0.8,0.6), apply the LRR model and then compute the pixel-wise maximum of predicted class conditional probability maps. Post-processing with the CRF yields small additional gains in performance. Fig. 7 reports the mean IoU for our LRR-4x model prediction when running at multiple scales and with the integration of the CRF. Fusing multiple scales yields a noticeable improvement (between 1.1% to 2.5%) while the CRF gives an additional gain (between 0.9% to 1.4%).

	mean	areo	bike	bird	boat	bottle	bus	car	cat	chair	cow	table	dog	horse	mbike	person	plant	sheep	sofa	train	tv
							Only using VOC training data														
FCN-8s[24]	62.2	76.8	34.2	68.9	49.4	60.3	75.3	74.7	77.6	21.4	62.5	46.8	71.8	63.9	76.5	73.9	45.2	72.4	37.4	70.9	55.1
Hypercol[15]	62.6	68.7	33.5	69.8	51.3	70.2	81.1	71.9	74.9	23.9	60.6	46.9	72.1	68.3	74.5	72.9	52.6	64.4	45.4	64.9	57.4
Zoom-out[25]	69.6	85.6	37.3	**83.2**	62.5	66.0	85.1	80.7	84.9	27.2	73.2	57.5	78.1	79.2	81.1	77.1	53.6	74.0	49.2	71.7	63.3
EdgeNet[4]	71.2	83.6	35.8	82.4	63.1	68.9	86.2	79.6	84.7	31.8	74.2	61.1	79.6	76.6	83.2	80.9	58.3	82.6	49.1	74.8	65.1
Attention[7]	71.5	86.0	38.8	78.2	63.1	70.2	89.6	84.1	82.9	29.4	75.2	58.7	79.3	78.4	83.9	80.3	53.5	82.6	51.5	79.2	64.2
DeepLab[5]	71.6	84.4	54.5	81.5	63.6	65.9	85.1	79.1	83.4	30.7	74.1	59.8	79.0	76.1	83.2	80.8	59.7	82.2	50.4	73.1	63.7
CRFRNN[37]	72.0	87.5	39.0	79.7	64.2	68.3	87.6	80.8	84.4	30.4	78.2	60.4	80.5	77.8	83.1	80.6	59.5	82.8	47.8	78.3	67.1
DeconvN[26]	72.5	89.9	39.3	79.7	63.9	68.2	87.4	81.2	86.1	28.5	77.0	62.0	79.0	80.3	83.6	80.2	58.8	83.4	54.3	80.7	65.0
DPN [23]	74.1	87.7	**59.4**	78.4	64.9	70.3	89.3	83.5	86.1	31.7	79.9	62.6	81.9	80.0	83.5	82.3	60.5	83.2	53.4	77.9	65.0
Adelaide[21]	75.3	90.6	37.6	80.0	67.8	**74.4**	92.0	85.2	86.2	**39.1**	81.2	58.9	83.8	83.9	84.3	**84.8**	**62.1**	83.2	**58.2**	80.8	**72.3**
LRR	74.7	89.2	40.3	81.2	63.9	73.1	91.7	86.2	87.2	35.4	80.1	62.4	82.6	84.4	84.8	81.7	59.5	83.6	54.3	83.7	69.3
LRR-CRF	**75.9**	**91.8**	41.0	83.0	62.3	74.3	**93.0**	**86.8**	**88.7**	36.6	**81.8**	**63.4**	**84.7**	**85.9**	**85.1**	83.1	62.0	**84.6**	55.6	**84.9**	70.0
							Using VOC and COCO training data														
EdgeNet[4]	73.6	88.3	37.0	**89.8**	63.6	70.3	87.3	82.0	87.6	31.1	79.0	61.9	81.6	80.4	84.5	83.3	58.4	86.1	55.9	78.2	65.4
CRFRNN[37]	74.7	90.4	55.3	88.7	68.4	69.8	88.3	82.4	85.1	32.6	78.5	64.4	79.6	81.9	86.4	81.8	58.6	82.4	53.5	77.4	70.1
BoxSup[10]	75.2	89.8	38.0	89.2	**68.9**	68.0	89.6	83.0	87.7	34.4	83.6	67.1	81.5	83.7	85.2	83.5	58.6	84.9	55.8	81.2	70.7
SBound[19]	75.7	90.3	37.9	89.6	67.8	74.6	89.3	84.1	89.1	35.8	83.6	66.2	82.9	81.7	85.6	84.6	60.3	84.8	60.7	78.3	68.3
Attention[7]	76.3	93.2	41.7	88.0	61.7	74.9	92.9	84.5	90.4	33.0	82.8	63.2	84.5	85.0	87.2	85.7	60.5	87.7	57.8	**84.3**	68.2
DPN [23]	77.5	89.0	**61.6**	87.7	66.8	74.7	91.2	84.3	87.6	36.5	86.3	66.1	84.4	87.8	85.6	85.4	63.6	87.3	61.3	79.4	66.4
Adelaide[21]	77.8	**94.1**	40.4	83.6	67.3	**75.6**	93.4	84.4	88.7	41.6	**86.4**	63.3	85.5	**89.3**	85.6	86.0	**67.4**	**90.1**	62.6	80.9	**72.5**
LRR	77.9	91.4	43.2	87.9	64.5	75.0	93.1	86.7	90.6	42.4	82.9	68.1	85.2	87.8	88.6	86.4	65.4	85.0	62.2	83.3	71.6
LRR-CRF	**78.7**	93.2	44.2	89.4	65.4	74.9	**93.9**	**87.0**	**92.0**	**42.9**	83.7	**68.9**	**86.5**	88.0	**89.0**	**87.2**	67.3	85.6	**64.0**	84.1	71.5
							ResNet + Using VOC and COCO training data														
DeepLab[6]	**79.7**	**92.6**	**60.4**	91.6	63.4	**76.3**	95.0	88.4	**92.6**	32.7	**88.5**	67.6	**89.6**	**92.1**	87.0	**87.4**	63.3	**88.3**	**60.0**	**86.8**	74.5
LRR	78.7	90.8	44.4	94.0	**65.8**	75.8	94.4	88.6	91.4	**39.1**	84.7	70.0	87.5	88.7	88.3	85.8	64.1	85.6	56.6	85.1	76.8
LRR-CRF	79.3	92.4	45.1	**94.6**	65.2	75.8	**95.1**	**89.1**	92.3	39.0	85.7	**70.4**	88.6	89.4	**88.6**	86.6	**65.8**	86.2	57.4	85.7	**77.3**

Fig. 9. Per-class mean intersection-over-union (IoU) performance on PASCAL VOC 2012 segmentation challenge test data. We evaluate models trained using only VOC training data as well as those trained with additional training data from COCO. We also separate out a high-performing variant built on the ResNet-101 architecture.

5.5   Benchmark Performance

PASCAL VOC Benchmark: As the Table 9 indicates, the current top performing models on PASCAL all use additional training data from the MS COCO dataset [22]. To compare our approach with these architectures, we also pretrained versions of our model on MS COCO. We utilized the 20 categories in COCO that are also present in PASCAL VOC, treated annotated objects from other categories as background, and only used images where at least 0.02% of the image contained PASCAL classes. This resulted in 97765 out of 123287 images of COCO training and validation set.

Training was performed in two stages. In the first stage, we trained LRR-32x on VOC images and COCO images together. Since, COCO segmentation annotations are often coarser in comparison to VOC segmentation annotations, we did not use COCO images for training the LRR-4x. In the second stage, we used only PASCAL VOC images to further fine-tune the LRR-32x and then added in connections to the 16x, 8x and 4x layers and continue to fine-tune. We used the multi-scale data augmentation described in section 5.1 for both stages. Training on this additional data improved the mean IoU of our model from 74.6% to 77.5% on PASCAL VOC 2011 validation set (see Table 7).

Cityscapes Benchmark: The Cityscapes dataset [8] contains high quality pixel-level annotations of images collected in street scenes from 50 different cities. The training, validation, and test sets contain 2975, 500, and 1525 images re-

	unmasked+DE	masked+DE
LRR-4x(32x)	64.7%	64.7%
LRR-4x(16x)	66.7%	67.1%
LRR-4x(8x)	68.5%	69.3%
LRR-4x	68.9%	70.0%

(a)

	IoU class	iIoU class	IoU cat	iIoU cat
FCN-8s [24]	65.3%	41.7%	85.7%	70.1%
CRF-RNN [37]	62.5%	34.4%	82.7%	66.0%
Dilation10 [34]	67.1%	42.0%	86.5%	71.1%
DPN [23]	66.8%	39.1%	86.0%	69.1%
Pixel-level Encoding [30]	64.3%	41.6%	85.9%	73.9%
DeepLab(ResNet) [6]	70.4%	42.6%	86.4%	67.7%
Adelaide_Context [21]	**71.6%**	**51.7%**	87.3%	74.1%
LRR-4x(VGG16)	69.7%	48.0%	**88.2%**	**74.7%**

(b)

Fig. 10. (a) Mean intersection-over-union (IoU class) accuracy on Cityscapes validation set for intermediate outputs at different levels of our Laplacian reconstruction architecture trained with and without boundary masking. (b) Comparison of our model with state-of-the-art methods on the Cityscapes benchmark test set.

spectively (we did not use coarse annotations). This dataset contains labels for 19 semantic classes belonging to 7 categories of ground, construction, object, nature, sky, human, and vehicle.

The images of Cityscapes are high resolution (1024×2048) which makes training challenging due to limited GPU memory. We trained our model on a random crops of size 1024×512. At test time, we split each image to 2 overlapping windows and combined the predicted class probability maps. We did not use any CRF post-processing on this dataset. Fig. 10 shows evaluation of our model built on VGG-16 on the validation and test data. It achieves competitive performance on the test data in comparison to the state-of-the-art methods, particularly on the category level benchmark. Examples of semantic segmentation results on the validation images are shown in Fig. 11

6   Discussion and Conclusions

We have presented a system for semantic segmentation that utilizes two simple, extensible ideas: (1) sub-pixel upsampling using a class-specific reconstruction basis, (2) a multi-level Laplacian pyramid reconstruction architecture that uses multiplicative gating to more efficiently blend semantic-rich low-resolution feature map predictions with spatial detail from high-resolution feature maps. The resulting model is simple to train and achieves performance on PASCAL VOC 2012 test and Cityscapes that beats all but two recent models that involve considerably more elaborate architectures based on deep CRFs. We expect the relative simplicity and extensibility of our approach along with its strong performance will make it a ready candidate for further development or direct integration into more elaborate inference models.

Fig. 11. Examples of semantic segmentation results on PASCAL VOC 2011 (top) and Cityscapes (bottom) validation images. For each row, we show the input image, ground-truth and the segmentation results of intermediate outputs of our LRR-4x model at the 32x, 16x and 8x layers. For the PASCAL dataset we also show segmentation results of FCN-8s [24].

References

1. Burt, P.J., Adelson, E.H.: The laplacian pyramid as a compact image code. IEEE Transactions on Communications 31(4), 532–540 (1983)
2. Carreira, J., Li, F., Sminchisescu, C.: Object recognition by sequential figure-ground ranking. IJCV 98(3), 243–262 (2012)
3. Carreira, J., Sminchisescu, C.: CPMC: Automatic object segmentation using constrained parametric min-cuts. PAMI 34(7), 1312–1328 (2012)
4. Chen, L.C., Barron, J.T., Papandreou, G., Murphy, K., Yuille, A.L.: Semantic image segmentation with task-specific edge detection using cnns and a discriminatively trained domain transform. In: CVPR (2016)
5. Chen, L.C., Papandreou, G., Kokkinos, I., Murphy, K., Yuille, A.L.: Semantic image segmentation with deep convolutional nets and fully connected crfs. In: ICLR (2015)
6. Chen, L.C., Papandreou, G., Kokkinos, I., Murphy, K., Yuille, A.L.: Deeplab: Semantic image segmentation with deep convolutional nets, atrous convolution, and fully connected crfs. arXiv preprint arXiv:1606.00915 (2016)
7. Chen, L.C., Yang, Y., Wang, J., Xu, W., Yuille, A.L.: Attention to scale: Scale-aware semantic image segmentation. In: CVPR (2015)
8. Cordts, M., Omran, M., Ramos, S., Rehfeld, T., Enzweiler, M., Benenson, R., Franke, U., Roth, S., Schiele, B.: The cityscapes dataset for semantic urban scene understanding. In: CVPR (2016)
9. Dai, J., He, K., Sun, J.: Convolutional feature masking for joint object and stuff segmentation. arXiv preprint arXiv:1412.1283 (2014)
10. Dai, J., He, K., Sun, J.: Boxsup: Exploiting bounding boxes to supervise convolutional networks for semantic segmentation. In: ICCV. pp. 1635–1643 (2015)
11. Denton, E.L., Chintala, S., Fergus, R., et al.: Deep generative image models using a laplacian pyramid of adversarial networks. In: NIPS. pp. 1486–1494 (2015)
12. Everingham, M., Eslami, S.A., Van Gool, L., Williams, C.K., Winn, J., Zisserman, A.: The pascal visual object classes challenge: A retrospective. IJCV pp. 98–136 (2015)
13. Gidaris, S., Komodakis, N.: Object detection via a multi-region and semantic segmentation-aware cnn model. In: ICCV. pp. 1134–1142 (2015)
14. Hariharan, B., Arbeláez, P., Bourdev, L., Maji, S., Malik, J.: Semantic contours from inverse detectors. In: ICCV. pp. 991–998 (2011)
15. Hariharan, B., Arbeláez, P., Girshick, R., Malik, J.: Hypercolumns for object segmentation and fine-grained localization. In: CVPR. pp. 447–456 (2015)
16. He, K., Zhang, X., Ren, S., Sun, J.: Deep residual learning for image recognition. arXiv preprint arXiv:1512.03385 (2015)
17. He, K., Zhang, X., Ren, S., Sun, J.: Identity mappings in deep residual networks. In: ECCV (2016)
18. Kohli, P., Ladicky, L., Torr, P.H.: Robust higher order potentials for enforcing label consistency. IJCV 82(3), 302–324 (2009)
19. Kokkinos, I.: Pushing the boundaries of boundary detection using deep learning. In: ICLR (2016)
20. Krähenbühl, P., Koltun, V.: Efficient inference in fully connected crfs with gaussian edge potentials. In: NIPS (2011)
21. Lin, G., Shen, C., Hengel, A.v.d., Reid, I.: Efficient piecewise training of deep structured models for semantic segmentation. In: CVPR (2016)

22. Lin, T.Y., Maire, M., Belongie, S., Hays, J., Perona, P., Ramanan, D., Dollár, P., Zitnick, C.L.: Microsoft coco: Common objects in context. In: ECCV. pp. 740–755 (2014)
23. Liu, Z., Li, X., Luo, P., Loy, C.C., Tang, X.: Semantic image segmentation via deep parsing network. In: ICCV. pp. 1377–1385 (2015)
24. Long, J., Shelhamer, E., Darrell, T.: Fully convolutional networks for semantic segmentation. In: CVPR. pp. 3431–3440 (2015)
25. Mostajabi, M., Yadollahpour, P., Shakhnarovich, G.: Feedforward semantic segmentation with zoom-out features. In: CVPR. pp. 3376–3385 (2015)
26. Noh, H., Hong, S., Han, B.: Learning deconvolution network for semantic segmentation. In: ICCV. pp. 1520–1528 (2015)
27. Pinheiro, P.O., Lin, T.Y., Collobert, R., Dollár, P.: Learning to refine object segments. In: ECCV (2016)
28. Shotton, J., Winn, J., Rother, C., Criminisi, A.: Textonboost for image understanding: Multi-class object recognition and segmentation by jointly modeling texture, layout, and context. IJCV 81(1), 2–23 (2009)
29. Simonyan, K., Zisserman, A.: Very deep convolutional networks for large-scale image recognition. arXiv preprint arXiv:1409.1556 (2014)
30. Uhrig, J., Cordts, M., Franke, U., Brox, T.: Pixel-level encoding and depth layering for instance-level semantic labeling. arXiv preprint arXiv:1604.05096 (2016)
31. Vedaldi, A., Lenc, K.: Matconvnet – convolutional neural networks for matlab. In: ICML (2015)
32. Xie, S., Tu, Z.: Holistically-nested edge detection. In: ICCV. pp. 1395–1403 (2015)
33. Yang, S., Ramanan, D.: Multi-scale recognition with dag-cnns. In: ICCV. pp. 1215–1223 (2015)
34. Yu, F., Koltun, V.: Multi-scale context aggregation by dilated convolutions. arXiv preprint arXiv:1511.07122 (2015)
35. Zeiler, M.D., Fergus, R.: Visualizing and understanding convolutional networks. In: ECCV. pp. 818–833 (2014)
36. Zeiler, M.D., Taylor, G.W., Fergus, R.: Adaptive deconvolutional networks for mid and high level feature learning. In: ICCV. pp. 2018–2025 (2011)
37. Zheng, S., Jayasumana, S., Romera-Paredes, B., Vineet, V., Su, Z., Du, D., Huang, C., Torr, P.H.: Conditional random fields as recurrent neural networks. In: ICCV. pp. 1529–1537 (2015)